



HAL
open science

An effective combination reaction involved with sputtered and selenized Sb precursors for efficient Sb₂Se₃ thin film solar cells

Y.-D. Luo, R. Tang, S. Chen, J.-G. Hu, Y.-K. Liu, Y.-F. Li, X.-S. Liu, Z.-H. Zheng, Z.-H. Su, X.-F. Ma, et al.

► To cite this version:

Y.-D. Luo, R. Tang, S. Chen, J.-G. Hu, Y.-K. Liu, et al.. An effective combination reaction involved with sputtered and selenized Sb precursors for efficient Sb₂Se₃ thin film solar cells. Chemical Engineering Journal, 2020, 393, pp.124599. 10.1016/j.cej.2020.124599 . hal-02536592

HAL Id: hal-02536592

<https://univ-rennes.hal.science/hal-02536592>

Submitted on 4 May 2020

HAL is a multi-disciplinary open access archive for the deposit and dissemination of scientific research documents, whether they are published or not. The documents may come from teaching and research institutions in France or abroad, or from public or private research centers.

L'archive ouverte pluridisciplinaire **HAL**, est destinée au dépôt et à la diffusion de documents scientifiques de niveau recherche, publiés ou non, émanant des établissements d'enseignement et de recherche français ou étrangers, des laboratoires publics ou privés.

An effective combination reaction involved with sputtered and selenized Sb precursors for efficient Sb_2Se_3 thin film solar cells

Yan-Di Luo^{1#}, Rong Tang^{1#}, Shuo Chen^{1#}, Ju-Guang Hu¹, Yi-Ke Liu², Ying-Fen Li², Xin-Sheng Liu³, Zhuang-Hao Zheng¹, Zheng-Hua Su¹, Xiu-Fang Ma¹, Ping Fan¹, Xiang-Hua Zhang⁴, Hong-Li Ma⁴, Zhi-Gang Chen⁵, Guang-Xing Liang^{1*}

¹ Shenzhen Key Laboratory of Advanced Thin Films and Applications, Key Laboratory of Optoelectronic Devices and Systems of Ministry of Education and Guangdong Province, College of Physics and Optoelectronic Engineering, Shenzhen University, Shenzhen 518060, P. R. China

² School of Material and Metallurgical Engineering, Guizhou Institute of Technology, Guiyang 550003, P. R. China

³ Key Laboratory for Special Functional Materials of Ministry of Education, Henan University, Kaifeng 475004, P. R. China

⁴ Univ Rennes, CNRS, ISCR (Institut des Sciences Chimiques de Rennes) UMR6226, Rennes F-35000, France

⁵ Centre for Future Materials, University of Southern Queensland, Springfield Central, Brisbane, Queensland, 4300, Australia

Yan-Di Luo, Rong Tang, and Shuo Chen contributed equally.

*Corresponding author: Email: lgx@zu.edu.cn (Prof. Liang)

Keywords: Sb_2Se_3 solar cell; Magnetron sputtering; Selenization; Combination reaction; DFT calculations

Abstract: Sputtering followed by post annealing is extensively used for fabrication of copper indium gallium selenide (CIGS), copper zinc tin sulfide (CZTS) and copper zinc tin sulfur selenide (CZTSSe) thin film solar cells. In this work, Sb_2Se_3 as an emerging alternative absorber was fabricated by an effective combination reaction of annealing sputtered Sb metallic precursors under Se vapor. Self-assembled growth of Sb_2Se_3 thin films consist of large grains that across the whole films have been successfully fulfilled via this combination reaction.

Sb_2Se_3 thin films with desired orientation, stoichiometric composition and high-quality $\text{Sb}_2\text{Se}_3/\text{CdS}$ heterojunction could be achieved once a proper selenization scenario was employed. Further, by selecting Sb films as precursors, the thickness of interfacial MoSe_2 located at the back-contact region can be well controlled, leading to a significant enhancement in fill factor (FF) of the devices. This is in good accordance with our DFT simulation results which demonstrated Se vapor would be prone to react with the Sb lattice thermodynamically and thus limiting the thickness of the MoSe_2 layer. Finally, a champion Sb_2Se_3 thin film solar cell with power conversion efficiency of 6.15% was achieved, which represents the highest efficiency of sputtered Sb_2Se_3 solar cells.

1. Introduction

Thin film photovoltaics has been developed rapidly during the last decade as the power conversion efficiencies (PCE) of state-of-the-art thin film solar cells have already caught up with that of crystalline silicon solar cells.^[1-3] Cadmium telluride (CdTe) is one of the most well-developed thin film technologies due to its high device efficiency and low cost. However, the toxicity of Cd might hinder its further application since trends are moving to abundant and non-toxic materials for thin film photovoltaics. Antimony selenide (Sb_2Se_3) is regarded as an emerging non-toxic alternative absorber material to CdTe . Sb_2Se_3 is also a binary compound with only one stable phase. Further, it possesses excellent optoelectronic properties such as ideal optical bandgap (1.2 eV), high absorption coefficient ($>10^5 \text{ cm}^{-1}$) and decent carrier mobility ($\sim 10 \text{ cm}^2\text{V}^{-1}\text{s}^{-1}$).^[4-6] Moreover, the elemental compositions of Sb and Se, are both non-toxic and earth-abundant, suggesting a bright future of Sb_2Se_3 photovoltaic for high-efficiency performance and low-cost manufacturing.

Sb_2Se_3 crystals are composed of one-dimensional $(\text{Sb}_4\text{Se}_6)_n$ ribbons stacking vertically on the substrate via strong covalent Sb-Se bonds whilst in the [010] and [100] directions the ribbons are bonded together by weak van der Waals forces.^[7] Photogenerated carriers are

believed to be able to travel along the one-dimensional vertically oriented ribbons effectively. On the other hand, carrier transport would be much more difficult in the horizontal directions such as [010] and [100] since the carriers would have to hop across the barriers between ribbons. Therefore, crystal orientation has become an essential issue in high-efficiency Sb_2Se_3 thin film solar cell fabrication. Various thin film deposition techniques have been applied to fabricate highly optimized Sb_2Se_3 absorber layer, such as solution method,^[8-11] thermal evaporation,^[7, 12-15] vapor transport deposition (VTD),^[16-18] close spaced sublimation (CSS)^[6, 19,20] and sputtering.^[21, 22] To date, the highest PCE of Sb_2Se_3 thin film solar cells in the substrate and superstrate configurations are 9.2%^[19] and 7.6%,^[16] respectively, where CSS and VTD methods were utilized to tune the crystal orientation and crystallinity of the Sb_2Se_3 absorber layer precisely. Interface engineering was also conducted in Sb_2Se_3 devices as attempts have been made by introducing additional buffer layers to passivate defects at the heterojunction.^[9, 18, 23] However, it is widely accepted that a perfected light absorber layer still plays the most important role in Sb_2Se_3 photovoltaics.

Among the above-mentioned deposition techniques, magnetron sputtering is a well-established approach that has been extensively utilized in preparation of conventional efficient thin film solar cells such as copper indium gallium selenide (CIGS), copper zinc tin sulfide (CZTS) and copper zinc tin sulfur selenide (CZTSSe).^[24-26] Unlike other deposition techniques that could possibly lead to impurity introduction and material waste, magnetron sputtering has the advantages of precise composition control, excellent uniformity and simple experimental setup. So far, most of Sb_2Se_3 devices with top PCEs were fabricated by thermal evaporation, VTD and CSS techniques. Only a few efforts have been put on the investigation of magnetron sputtered Sb_2Se_3 thin films, thus further research would enable a bench mark to be established and provides a bright future to improve the overall performance of Sb_2Se_3 thin film solar cells. Recently, we have reported a Sb_2Se_3 thin film solar cell with PCE of 6.06% fabricated via magnetron sputtering followed by a post-selenization process.^[27] [211]-oriented Sb_2Se_3 thin

films with decent crystallinity were successfully prepared under an optimized selenization scenario after sputtered from a Sb_2Se_3 compound target. The final device presents a competitive short circuit current (J_{SC}) of 25.91 mA/cm² and open circuit voltage (V_{OC}) of 494 mV. However, compared to other highly efficient Sb_2Se_3 solar cells, the fill factor (FF) of this device is relatively poor with a value of 47.7%.

Post-annealing treatment of metallic precursors is an effective approach to fabricate efficient chalcogenide thin film solar cells such as CIGS, CZTSe and CZTSSe.^[28-30] The method enjoys the merit of accurate control of morphology and composition simultaneously. Enhanced crystallinity and larger grains of the absorbing thin films could be achieved by careful optimization of the annealing process. In this work, a combination reaction was utilized by annealing sputtered Sb metallic precursors under Se atmosphere to produce crystallized Sb_2Se_3 . In order to prepare Sb_2Se_3 thin films with desired orientation and crystallinity, the selenization process was thoroughly adjusted and investigated. Self-assembled growth of Sb_2Se_3 thin films consist of large grains whose sizes are equivalent to the thickness of the films has been successfully fulfilled via this combination reaction. The method has distinct advantages over the one in our last report where amorphous Sb_2Se_3 thin films were sputtered and selenized to produce the crystallized absorber layers. Firstly, selenization of the Sb metallic precursor would facilitate delicate control of the thin film key parameters such as orientation, chemical composition and crystallinity etc. Second, rather than using an expensive Sb_2Se_3 alloy sputtering target, a more economical Sb metallic target was chosen for this work. Moreover, the thickness of MoSe_2 interfacial layer at the back-contact region could be substantially reduced, leading to a significant recombination inhibition at the $\text{Sb}_2\text{Se}_3/\text{MoSe}_2$ interface thus a great FF improvement. Finally, a champion Sb_2Se_3 thin film solar cell with PCE of 6.15% was achieved, which represents the highest efficiency of sputtered Sb_2Se_3 solar cells.

2. Experimental Section

Deposition of Sb₂Se₃ thin film

Sb metallic precursors were deposited using a radiofrequency (RF) magnetron sputtering deposition system. High-purity Sb powder (>99.99%) purchased from HZAM (Beijing, China) was ball milled for 8 hours at a speed of 300 rpm/min and then sintered to prepare a dense Sb sputtering target (diameter of 60 mm and thickness of 2 mm) by Labox-325 SPS with a fixed pressure of 30 KN and temperature of 350 °C. Prior to sputtering deposition, Mo-coated glass substrates were subsequently cleaned in an ultrasonic bath using detergent, ethanol and deionized water. The background pressure of the sputtering vacuum chamber was evacuated below 7.0×10^{-4} Pa before the sputtering procedure commenced. Ar with high purity (>99.999%) was introduced into the sputtering chamber at a flow rate of 40 sccm. The working pressure and sputtering power were kept at 0.5 Pa and 30 W during the sputtering process, respectively. The sputtering duration was fixed at 60 min without additional *in-situ* heat treatment to obtain Sb metallic precursor with thickness of approximately 600 nm. Post-selenization procedures were subsequently carried out to prepare crystallized Sb₂Se₃ thin films (the details of the selenization process will be discussed later).

Device fabrication

Cadmium sulfide (CdS) buffer layer was deposited onto the crystallized Sb₂Se₃ thin films using chemical bath deposition (CBD) once the selenization process was finished. Cadmium sulfate (3CdSO₄·8H₂O) powder, thiourea powder and ammonium hydroxide aqueous solution (28%) were purchased from Aladdin (Shanghai, China). CdSO₄ aqueous solution (0.015 M), thiourea aqueous solution (0.75 M) and ammonium hydroxide aqueous solution were subsequently added to deionized water. The substrates were soaked into the mixed solution which was then placed in an 80 °C water bath under continuous stirring for 9 min. The substrates were rinsed with deionized water and dried in an oven. Indium tin oxide (ITO) thin film was then magnetron sputtered as a window layer. The device surface was scribed into small squares with identical area by knife and Ag electrodes were deposited onto the ITO surface via thermal evaporation

to form metallic contact (active area of each device = 0.15 cm²). A substrate configuration of Mo/Sb₂Se₃/CdS/ITO/Ag was assembled for our Sb₂Se₃ solar cells. The schematic diagram of the whole process of the Sb₂Se₃ thin film solar cell fabrication is illustrated in Figure 1.

Characterization of the Sb₂Se₃ films and devices

Surface and cross-sectional microstructures of the Sb₂Se₃ films were characterized using a scanning electron microscope (SEM, SUPRA 55). Crystal orientations of the Sb₂Se₃ films were studied by X-ray diffraction (XRD, Ultima-iv, CuK_α radiation under operation conditions of 40 kV and 40 mA from 10° to 60°). Chemical compositions of the films were analyzed using an energy dispersive X-ray spectroscope (EDS, BRUKER QUANTAX 200) equipped with the SEM. The current density–voltage (*J-V*) curves of the Sb₂Se₃ devices were measured under 100 mW/cm² AM 1.5 G light illumination using a class AAA solar simulator at room temperature. The external quantum efficiency (EQE) spectra were measured using a Zolix SCS101 system and a Keithley 2400 source meter. Transmission electron microscope (TEM) images were taken using a FEI Titan Cubed Themis G2 300 microscope. The sample for TEM imaging was prepared by ablating the thin film device using focused ion beam (FIB, FEI Scios). Temperature-dependent *V*_{OC} measurements were carried out using a Lakeshore 325 temperature controller and the temperatures were swept from 350 K to 120 K in a step of 30 K. During the measurements, the devices were mounted inside a Janis VPF-100 cryostat and cooled with liquid nitrogen. Capacitance-voltage (*C-V*) measurements were conducted at AC amplitude of 30 mV and frequency of 10 kHz under a dark condition at room temperature. The DC bias voltage during the *C-V* measurements was applied from -1 V to 0.3 V. Drive level capacitance profiling (DLCP) measurements were performed with an AC amplitude from 20 mV to 140 mV and a DC bias voltage from -0.2 V to 0.2 V. Temperature-dependent capacitance-frequency (*C-f-T*) measurements were carried out within the frequency range of 1 kHz to 10 MHz using the same cryostat and cooling system as mentioned above.

Density functional theory (DFT) calculation methods

DFT calculations were carried out using VASP5.3,^[31, 32] with the all-electron projector augmented wave (PAW) method.^[33, 34] The exchange-correlation effects were described by the generalized gradient approximation in form of Perdew-Burke-Ernzerh.^[35] The wave functions were expanded in a basis of plane waves with a kinetic energy cutoff of 520 eV and a density cutoff of 900 eV. Three-dimensional 54-atom periodic supercells with (3×3×3) and (3×3×1) unit cells were utilized for simulations of the bulk Mo and Sb systems, respectively. The corresponding Brillouin zone was sampled by (3×3×3) and (2×2×2) Gamma-centered Monkhorst-Pack grid meshes for the bulk Mo and Sb, respectively.^[36-38] Equilibrium cell volumes and all internal atomic positions of the supercells were fully relaxed until convergence with the total energy tolerance of 10⁻⁴ eV. The calculated lattice constants for bulk Mo and Sb were 3.16 Å and 4.37 Å/11.59 Å respectively, which agrees well with the experiments (3.15 Å and 4.31 Å/11.27 Å).^[38, 39] For the doped system, one Mo (or Sb) atom was substituted by the Se atom in the 54-atom supercells, and other parameters used are the same as for the pure bulk system. The Se atom was modeled in a (15 Å×15.1 Å×15.2 Å) unit cell, using only the Gamma point in k-space.

3. Results and Discussions

A schematic diagram of the whole process of the Sb₂Se₃ thin film solar cell fabrication is illustrated in Figure 1. Herein, the important combination reaction involved with sputtered and selenized Sb precursors have been investigated thoroughly. Homogeneous Sb metallic precursors were deposited onto Mo-coated glasses after careful optimization of the sputtering process. Subsequently, the sputtered precursors and 0.25 g of selenium (Se) powder with high purity (>99.99%) were separately placed into the two chambers of a vacuum tubular furnace for selenization. The chambers were evacuated using a mechanical pump before introducing high-purity Ar gas. During the annealing process, the working pressure and the Se powder side temperature were kept at 5×10⁴ Pa and 400 °C, respectively whilst the Sb precursor side temperature and the selenization duration were carefully adjusted to obtain the Sb₂Se₃ thin films

with desired orientation and crystallinity. Both the Se powder side temperature and the Sb precursor side temperature were ramped up to the set values at a heating rate of 20 °C/min. The furnace was naturally cooled down to room temperature once the selenization was finished. Substrate temperature has been proven as a crucial factor for perfecting morphology of Sb_2Se_3 thin films in our previous report.^[27] Therefore, the effect of substrate temperature on the Sb_2Se_3 thin film morphology and device performance was firstly investigated by varying the Sb metallic side temperature from 325 °C to 425 °C. The surface morphologies and chemical compositions of the Sb_2Se_3 thin films annealed at different temperatures are presented in Figure S1 (Supporting Information). Apparently, the grain sizes of the Sb_2Se_3 thin films are increased, indicating an evolution of crystallization and growth with increasing selenization temperature. The films were poorly crystallized when annealed at temperatures below 400 °C as small Sb_2Se_3 grains could be found all over the sample surface. Afterwards, the higher temperature could provide sufficient mobility for the Sb_2Se_3 molecules to pack together and facilitate the formation of larger Sb_2Se_3 grains. As a result, Sb_2Se_3 grains as large as 2 μm were formed when selenization process was carried out at 400 °C and 425 °C. The chemical composition of the thin film annealed at 400 °C is very close to its stoichiometric ratio (0.67). However, it can also be found that Sb_2Se_3 thin film annealed at 425 °C is severely Se-poor with a Sb/Se ratio as high as 0.73. We attribute this to the excessive annealing temperature that accelerated the evaporation rate of Se. It is reported that weight loss would start to occur from about 423 °C for Sb_2Se_3 and both Sb_2Se_3 and Se demonstrate very high vapor pressures at temperatures above 400 °C.^[12] Annealing the substrate at 425 °C would increase the extraction rate of Se from Sb_2Se_3 , leading to the formation of Se vacancy defects and thus deteriorating the device performance. The performances of Sb_2Se_3 devices fabricated at different selenization temperatures are summarized in Figure S2 (Supporting Information) and Table S1 (Supporting Information), among them, the one selenized at 400 °C presents the highest PCE of 2.6%.

After analyzing the temperature effect, a range of selenization durations were selected to further optimize the Sb_2Se_3 thin film quality. The Sb precursor side temperature was fixed at 400 °C for each selenization scenario whilst the annealing duration was varied from 5 min to 30 min at an interval of 5 min. The SEM top-view images as well as the Sb/Se ratios of the Sb_2Se_3 thin films annealed at various selenization temperatures are shown in Figure 2. Prominent Sb_2Se_3 grain size development can be observed for the range of selenization duration from 5 min to 15 min, indicating the rapid growth of Sb_2Se_3 crystals at the beginning stage of selenization. Prolonged annealing treatment did not bring a notable effect on crystallization as the Sb_2Se_3 grain sizes are almost constant. Moreover, it should be noted that insufficient or over extended annealing time would deviate the thin films from stoichiometric composition, making the samples become Se-poor or Se-rich, respectively. An optimal Sb/Se ratio of 0.67 could be obtained under selenization duration of 15 min.

XRD results of Sb_2Se_3 thin films fabricated by various selenization scenarios are given in Figure 3a and Figure 3b. All the samples present a [221] preferred orientation which has been proven to be beneficial for carrier transport. [7, 15, 16] Herein, texture coefficient (TC), an indicator of preferred crystal orientation, is applied on the (221) diffraction peak to quantitatively investigate the orientation preference along this particular direction. The TC values were calculated based on the following equation [15]:

$$TC_{hkl} = \frac{I_{(hkl)}}{I_{0(hkl)}} / \left(\frac{1}{N} \sum_{i=1}^N \frac{I_{(h_i k_i l_i)}}{I_{0(h_i k_i l_i)}} \right) \quad (1)$$

where $I_{(hkl)}$ and $I_{0(hkl)}$ are the diffraction peak intensities of (hkl) planes in the measured and standard XRD pattern of Sb_2Se_3 (JCPDS 15-0861), respectively. Large TC value of a diffraction peak indicates preferred orientation along this particular direction.[15] It shows that the evolutions of (221) diffraction peaks (Figure 3c) and PCE (Figure 3d) of the Sb_2Se_3 thin film solar cells follow the same trend where the optimized condition could be obtained once the selenization was conducted at 400 °C for 15 min (15min- Sb_2Se_3). Consistent with efficient

Sb_2Se_3 thin film devices manufactured via other deposition techniques,^[16, 19, 23] the PCE of our devices correlates strongly with the orientation and crystallinity of the Sb_2Se_3 absorber layer. The current density-voltage (J - V) curves and detailed performance parameters of the Sb_2Se_3 devices with different selenization durations are summarized in Figure 4a and Table 1. A competitive PCE of 6.15 % was achieved for the 15min- Sb_2Se_3 device with the key device parameters namely, short circuit current density (J_{SC}), open circuit voltage (V_{OC}) and fill factor (FF) being 22.75 mA/cm², 455 mV and 59.5 %, respectively. 100 devices for both the 15min- Sb_2Se_3 and 20min- Sb_2Se_3 categories were tested to study the reproducibility of the devices and the main parameter boxplots of the two categories are illustrated in Supplementary Fig. S3. From the data it is clear that insufficient and over extended annealing durations would both bring a detrimental effect on the device performance. The external quantum efficiency (EQE) of the devices are provided in Figure 4b. The EQE responses demonstrate a dramatic decrease below approximately 520 nm which could be due to parasitic absorption of the CdS buffer layer. The 15min- Sb_2Se_3 device presents a substantially improved EQE at the visible region (400-750 nm) compared with the other devices, implying less recombination losses both at the $\text{Sb}_2\text{Se}_3/\text{CdS}$ interface and in the bulk film.^[39] We attribute this to the proper selenization process that not only passivated bulk defects but improved the adhesion at the heterojunction interface. At the longer wavelength region (800-1100 nm), the photo response of the 15min- Sb_2Se_3 device is also far stronger than that of the other devices, indicating less back interface recombination that originated from the micro-voids and small grains at the $\text{MoSe}_2/\text{Sb}_2\text{Se}_3$ interface in this particular device.^[40] The J - V measurements were also carried out for the 15 min- Sb_2Se_3 device using different scanning directions (Figure 4c) and obviously there is no hysteresis between the forward and backward scans as two J - V curves are overlapped perfectly. The champion device was placed in the ambient air without any special treatment/encapsulation for over 60 days to investigate the device stability. PCE of the device was measured every 5 days and the result is given in Figure 4d. The 15min- Sb_2Se_3 sample presented an outstanding device stability since

only a slight performance degradation could be seen with PCE decreased from 6.15 % to 5.46 % after long-term exposure to ambient air without any intentional storage.

In order to investigate the mechanisms of the improved performance of the 15min-Sb₂Se₃ device, dark J - V characteristics were carried out for both the 15min-Sb₂Se₃ and 20min-Sb₂Se₃ samples. Figure 5a shows the J - V curves of the two devices under dark condition. Shunt conductance (G), series resistance (R), diode ideality factor (A) and reverse saturation current density (J_0) of the two devices were calculated according to the Site's method,^[41] as in equation (2):

$$J = J_0 \exp \left[\frac{q}{AkT} (V - RJ) \right] + GV - J_L \quad (2)$$

The shunt conductance G were obtained as 2.1 and 5.2 mS/cm² for the 15min-Sb₂Se₃ and 20min-Sb₂Se₃ device respectively by extracting the flat regions of the plots of dJ/dV against V under reverse bias, as shown in Figure 5b. The series resistance (R) can be obtained by extrapolating the plots of dJ/dV against $(J+J_{SC})^{-1}$ to the Y -axis while the diode ideality factor (A) can be calculated as the slope of AkT/q (Figure 5c).^[42] The series resistance and diode ideality factor were calculated to be $R = 8.03 \Omega/\text{cm}^2$, $A = 1.86$ and $R = 11.61 \Omega/\text{cm}^2$, $A = 2.30$ for the 15min-Sb₂Se₃ and 20min-Sb₂Se₃ device respectively. The reverse saturation current density (J_0) can be acquired by plotting the $\ln(J+J_{SC}-GV)$ against $V-RJ$ (Figure 5d) and the resulted J_0 for the 15min-Sb₂Se₃ and 20min-Sb₂Se₃ device are 4.3×10^{-3} and 4.5×10^{-4} mA/cm², respectively. It can be concluded from the above results that a suitable selenization duration could greatly improve the Sb₂Se₃/CdS heterojunction quality of the device, as evidence by the much smaller values of J_0 and A for the 15min-Sb₂Se₃ sample. Moreover, the proper annealing time would also minimize the series resistance and thus enhancing the FF for the device.

The schematic diagram of the reaction and formation of Sb₂Se₃ thin films via selenization of Sb metallic precursors is illustrated in Figure 6. Sb metallic precursors were homogeneously deposited onto the Mo substrate using magnetron sputtering. The surface morphology of the as-

deposited precursor is nearly featureless with only ripple-like Sb grains can be spotted, suggesting amorphous nature for the precursor. Once the selenization started a large amount of Se atoms would diffuse and react with the Sb lattice to form Sb_2Se_3 molecules under high temperature condition. The reaction would take place gradually towards the Mo substrate where the Sb precursor thin film would be consumed and turned into Sb_2Se_3 from the surface to the bottom of the absorber layer. As a result, it can be predicted that selenization duration would play a key role in the Sb_2Se_3 layer preparation. A short period of annealing time would not only prevent further chemical combination of Se vapor and Sb lattice towards the Mo substrate, but leads to insufficient crystallization for the upper layer of the Sb_2Se_3 thin film. Grain size distributions of Sb_2Se_3 thin films at an early stage ($t = 5$ min) and later stage ($t = 15$ min) of selenization are given in Figure S4 (Supporting Information). Obviously, the average grain size of the Sb_2Se_3 thin film was significantly enhanced once a proper annealing time had been applied, which could effectively hinder recombination losses originated from the grain boundaries.

On the other hand, excessively prolonged annealing time would be harmful to the device performance as well. Figure 7 shows the SEM cross-sectional morphology of Sb metallic precursor selenized at 400°C for various annealing durations. It is seen that when the precursors were annealed for a relatively short period of time ($t = 5$ min and $t = 10$ min), small grains and voids appear at the bottom of the absorber layer owing to shallow Se diffusion. The sample annealed for 15 min (Figure 7c) is composed of large grains whose sizes are equivalent to the thickness of the absorber layer. Combined with the previous XRD results (Figure 3), it is suggested that self-assembled growth of Sb_2Se_3 thin films with significantly improved crystallinity and desired orientation have been achieved via sufficient combination reaction between the Sb metallic precursor and Se vapor under high temperature. In addition, the sample also shows good adhesion between the absorber layer and the back contact as no visible voids are present at the Mo/ Sb_2Se_3 interface. For the samples annealed over 15 min ($t = 20$ min, $t =$

25 min and $t = 30$ min), large voids can be clearly seen at the bottom of the Sb_2Se_3 layer, implying severe decomposition of the thin film materials due to over prolonged selenization durations. Such poor adhesion between the Sb_2Se_3 thin films and the Mo contact would significantly downgrade the carrier extraction ability and the device performance. In sum, highly crystalline stoichiometric Sb_2Se_3 thin films with [221] preferred orientation was fabricated through self-assembly via an effective combination reaction approach. Large Sb_2Se_3 grains with excellent continuity across the whole absorber layer as well as improved adhesion between the Sb_2Se_3 thin films and the Mo contact were achieved after careful optimization of the selenization process.

MoSe_2 or MoS_2 thin film layer is a common issue that has been extensively studied in many chalcogenide thin film solar cells such as CIGS, CZTSe, CZTSSe and Sb_2Se_3 in substrate configuration.^[40, 43-45] It has been reported that such an interfacial layer between the absorber layer and Mo substrate with appropriate thickness could decrease the back contact barrier to improve the carrier transport and reduce the recombination loss. However, an over-thick interlayer will dramatically increase the series resistance of the device, leading to deterioration in PCE. Given that the over-thick interlayer would be prone to form within those thin film devices that are fabricated via high temperature selenization or sulfurization, it is vital to optimize the annealing process to control the thickness of the interfacial layer within a desired range. Herein, cross-sectional morphology of the champion device was characterized by TEM (Figure 8a) to investigate the formation of the MoSe_2 interfacial layer. A thin interfacial layer with thickness less than 50 nm can be clearly observed between the Mo substrate and the Sb_2Se_3 layer. High-resolution transmission electron microscopy (HRTEM) imaging was performed at the $\text{Sb}_2\text{Se}_3/\text{CdS}$ junction (Figure 8b) and it is obvious the heterojunction is of high quality as smooth interface is present between the Sb_2Se_3 layer and CdS buffer layer without abrupt interfacial boundary. Further, lattice fringe distances of three arbitrary points a, b and c that were randomly selected near the top, middle and bottom regions of the Sb_2Se_3 thin film were

measured, as shown in Figure 8c-e. As can be seen from the results the distances between the lattice lines, namely 0.284 nm and 0.315 nm, which correspond to the (221) and (211) planes in Sb_2Se_3 , are highly consistent for the three measuring points. Such a vertical preferred crystal orientation across the whole Sb_2Se_3 film would facilitate facile charge carrier transport within the light absorber layer and thus improving the device performance.^[7] Energy dispersive spectroscopy (EDS) elemental profiles were then conducted for the 15min- Sb_2Se_3 and 20 min- Sb_2Se_3 sample to compare the MoSe_2 thickness of the two devices quantitatively (Figure 8f). For both devices, elemental profile crossover of Mo and Se could be found, implying the existence of MoSe_2 interfacial layer in the two devices. It should also be noted that the crossover region become broad as severe Mo and Se tails are apparent for the 20 min- Sb_2Se_3 devices, suggesting the thickness increase of the MoSe_2 layer due to prolonged annealing time. The over-thick MoSe_2 interfacial layer is believed to be responsible for the poor FF of the 20 min- Sb_2Se_3 device (49.8%). In addition, high-angle annular dark-field scanning transmission electron microscope (HAADF-STEM) equipped with EDS was performed for the champion device and no overlap phenomenon could be observed between the elemental mapping results of Mo and Se (Figure 8g), hinting that no or a very thin interfacial layer might exist between the Mo substrate and the absorber layer. To further explore the effect of the MoSe_2 interfacial layer in magnetron sputtered Sb_2Se_3 thin film solar cells, it is important to be reminded that the device of our previous work contained a relatively thick MoSe_2 layer (~ 200 nm)^[27], on the other hand a much thinner MoSe_2 thin film with thickness less than 50 nm is present in the device of this work. This prominent difference in MoSe_2 thickness can be attributed to fabrication variation of the two methods. In this project, crystallized Sb_2Se_3 thin film was prepared by selenization of Sb metallic precursors under high temperature. During the selenization process Se vapor would diffuse into the metallic precursor lattice and react with the Sb atoms. The combination reaction took place from the sample surface towards the bottom of the film, turning the Sb precursor into Sb_2Se_3 compound gradually. At the early stage of

selenization, the upper layer of the Sb precursor would be fully consumed and became Sb_2Se_3 compound, while leaving the lower layer unaffected. DFT calculations were conducted using VASP5.3, [31, 32] with the all-electron projector augmented wave (PAW) method [33, 34] in this work. When one Mo or Se atom was substituted by one Se atom in the periodic supercells, the energy change ΔE was calculated as $\Delta E = E_{\text{total}} + E_{\text{Mo(or Sb)}} - E_{\text{bulk}} - E_{\text{Se}}$, which is the energy gain with respect to the Se atom in the gas phase and the metal atoms in the bulk phase. E_{total} and E_{bulk} are the total energy of the doped system and the pure metal system in the periodic supercells, respectively. $E_{\text{Mo(or Sb)}}$ and E_{Se} are the calculated energy of one Mo (or Sb) atom in the bulk phase and one Se atom in the gas phase, respectively. Here a negative (positive) value indicates that the substitution is exothermic (endothermic). Our DFT calculations show that when 1/54 Sb atoms were substituted by Se atoms in the bulk Sb, the energy change is -2.54 eV, which is 1.31 eV lower than the corresponding process in the bulk Mo system (as shown in Figure S5, Supporting Information), suggesting the reaction between Se and Sb is energetically favorable than that between Se and Mo. As a result, Se vapor would preferentially react with the Sb precursor during the annealing process, and meanwhile, hinder the reaction with Mo substrate thus limiting the MoSe_2 thickness. Therefore, it is logical to presume the thickness of the MoSe_2 interfacial layer can be well controlled once a proper annealing duration is applied. However, the situation was quite different in our last work where amorphous Sb_2Se_3 thin films were used as precursors for post-selenization. Excessive Se vapor would penetrate through the Sb_2Se_3 thin film with ease, without being consumed and react with the Mo substrate. Moreover, the bottom part of the amorphous Sb_2Se_3 thin film that adjacent to the Mo substrate would be prone to evaporate under high temperature and produce even more Se vapor which could further facilitate the formation of MoSe_2 interlayer. As a consequence, an over-thick MoSe_2 interfacial layer is usually present in devices fabricated by post-selenization of Sb_2Se_3 amorphous thin films, introducing severe recombination at the $\text{Sb}_2\text{Se}_3/\text{MoSe}_2$ interface and significant FF deterioration of the device.

Efficiency records of planar heterojunction Sb_2Se_3 thin film solar cells in substrate configuration fabricated by various techniques are summarized in Table 2. It can be seen that our champion device with a highly interesting PCE of 6.15 % is comparable to the state-of-the-art devices and represents the highest efficiency of sputtered Sb_2Se_3 solar cells. Additionally, the competitive FF (59.5 %) of our champion device is really attributed to the ultrathin MoSe_2 interlayer, whose growth could be naturally hindered during the combination reaction of the sputtered and selenized Sb metallic precursors.

Capacitance-voltage (C - V) profiling and deep-level capacitance profiling ($DLCP$) characterizations were carried out to investigate interfacial properties of the devices (Figure 9a). In general, the C - V measured doping density (N_{C-V}) includes free carriers, bulk defects and interfacial defects, whilst the $DLCP$ measured doping density (N_{DLCP}) only represents responses from free carriers and bulk defects.^[46] Therefore, the interfacial defect density of the device can be calculated as the subtraction of N_{DLCP} from N_{C-V} . The plots of N_{C-V} and N_{DLCP} against the profiling depth x can be expressed as the following equations,

$$\left\{ \begin{array}{l} N_{C-V} = \frac{-2\varepsilon_{r,n}N_D}{\left(\frac{d(1/C^2)}{dV}\right)qA^2\varepsilon_0\varepsilon_{r,n}\varepsilon_{r,p}N_D + 2\varepsilon_{r,p}} \\ N_{DLCP} = -\frac{C_0^3}{2q\varepsilon_0\varepsilon_{r,p}A^2C_1} \\ x = \varepsilon_0\varepsilon_{r,p}A/C_0 \end{array} \right. \quad (3)$$

where $\varepsilon_{r,n}$ and $\varepsilon_{r,p}$ are the relative permittivity of CdS and Sb_2Se_3 , respectively, N_D is the doping density of CdS, A is the device area, C_0 and C_1 are two quadratic fitting parameters derived from the C - V curves. For the 20min- Sb_2Se_3 device, a gap can be clearly observed between the N_{C-V} and N_{DLCP} curves. However, the difference between the two curves is much smaller in the 15min- Sb_2Se_3 device, indicating lower defect density and less severe recombination at the $\text{Sb}_2\text{Se}_3/\text{CdS}$ heterojunction for the device. This could be attributed to the properly optimized selenization duration which could effectively passivate the interfacial defects originated from

dangling-bond-rich grain boundaries by producing more favorable orientation and crystallinity for the Sb_2Se_3 thin film. In addition, it should be noted that from Figure 9, the 15min- Sb_2Se_3 device possesses a wider depletion region, which might enhance light absorption and carrier extraction ability of the device.

To further investigate the dominant recombination type of our devices, temperature-dependent open circuit voltage (V_{OC} - T) measurements were undertaken from 400 K to 100 K and activation energy E_a of recombination processes of the devices can be calculated by extrapolating the V_{OC} to the Y-axis, as shown in Figure 9b. Both the devices possess an E_a a bit lower than the optical bandgap of the Sb_2Se_3 absorber (1.2eV, as estimated from the EQE data), implying the device performance losses were dominated by the Schottky-Read-Hall recombination in the depletion regions.^[40] The lower E_a suggests that there exists more serious interfacial recombination for the 20 min- Sb_2Se_3 device which might be originated from the over-thick MoSe_2 interfacial layer as well as poor adhesion between the Sb_2Se_3 absorber and Mo substrate due to the large voids at the Mo/ Sb_2Se_3 interface (Figure 7d). Electron beam-induced current (EBIC) measurements were conducted to explore the carrier collection efficiency of the devices (Figure 9c). As expected, light areas that indicating high collection efficiency regions locate at the $\text{Sb}_2\text{Se}_3/\text{CdS}$ interfaces for the both devices. Apparently, the light area of the 15min- Sb_2Se_3 device is wider than that of the 20 min- Sb_2Se_3 device, suggesting a longer depletion region for the 15min- Sb_2Se_3 device, which is consistent with the C - V measurement results. Furthermore, compared to the 15min- Sb_2Se_3 device, the 20min- Sb_2Se_3 device presents a light area with lower brightness, indicating significant carrier recombination possibly due to excessive interfacial defects, which echoes the observations of the C - V and $DLCP$ measurements. EBIC signals were scanned across the device for both the samples (Figure 9d), the signals were normalized to the maximum value and the decay rate of the 15min- Sb_2Se_3 device is slower than that of the 20min- Sb_2Se_3 device over the whole device, implying

a substantial enhancement of the carrier collection efficiency at both the front electrode and deep absorber.^[18]

Admittance spectroscopy has been regarded as a useful tool to investigate defect properties in conventional thin film solar cell characterizations.^[17, 47, 48] In order to get a deeper understand of distribution and density of defects as well as defect-induced carrier recombination mechanisms for our devices, temperature-dependent admittance (C - f - T) measurements were conducted in the temperature range of 180 to 330 K and the C - f - T spectra of our champion device (6.15%, 15 min-Sb₂Se₃) are demonstrated in Figure 10. Three peaks were distinguished from the $\omega dC/d\omega$ plots (not shown here) that could be ascribed to three defect levels, denoted as D1, D2 and D3 within our devices, which is consistent with defect characterizations of Sb₂Se₃ solar cells in literature.^[18] Angular frequency point ω at the maximum of the $\omega dC/d\omega$ plot was defined as the inflection point frequency ω_0 for each C - f - T curve. The defect activation energies (E_a) were derived from the slopes of the Arrhenius plots that were linearly fitted based on the equation:

$$\omega_0 = 2\pi\nu_0 T^2 \exp\left(\frac{-E_a}{kT}\right) \quad (4)$$

where ν_0 is the attempt-to-escape frequency, ω_0 is the inflection point frequency and E_a is the defect activation energy that represents the average energetic depth of the defect relative to the valence band maximum (VBM) or conduction band minimum (CBM).^[48] The distribution of each defect type was Gaussian fitted using the Kimerling model based on the following equation:

$$E(\omega) = kT \ln\left(\frac{2\pi\nu_0 T^2}{\omega}\right) \quad (5)$$

$$N_t(E(\omega)) = -\frac{V_d}{q\omega} \cdot \frac{dC}{d\omega} \cdot \frac{\omega}{kT} \quad (6)$$

where V_d is the built-in potential of the p-n junction, ω is the angular frequency and $N_t(E(\omega))$ is the defect density. The detailed defect parameters of the 15min-Sb₂Se₃ and 20min-Sb₂Se₃ devices are summarized in Table 3. Since our Sb₂Se₃ thin films were subjected to overabundant Se vapor during the selenization process due to the high vapor pressure of Se under elevated temperature, the Sb₂Se₃ films were slightly Se rich. DFT calculations have revealed that three types of intrinsic defects, namely, Sb vacancy V_{Sb} , Se_{Sb} antisite and Se interstitial Se_i , are dominating within Sb₂Se₃ devices that were fabricated under Se-rich growth conditions.^[49, 50] A small gap of activation energy is observed between the two devices for each defect level and thus it is legal to claim that the defect types are identical for the two devices. It is almost certain that D1 with lowest activation energy could be assigned to V_{Sb} defects, which are shallow acceptors that could be easily formed under Se-rich environments. D2, D3 with higher activation energies can be assigned to Se_i and Se_{Sb} defects respectively, according to the DFT simulation results.^[49] Although Se_i has a deep energy level, the defect ionization level is higher than the CBM. Hence it is unlikely for these defects act as recombination centers and their impacts on the performance losses of the devices are thus minimized. Since V_{Sb} are shallow acceptors with very low activation energy and given that the defect density is relatively low, the contribution of this defect state to the recombination losses will be limited as well. On the other hand, Se_{Sb} antisite has been reported as one of the dominant defect states for Sb₂Se₃ solar cells.^[16] Due to the high activation energy, the energy level of Se_{Sb} defects is quite close to the midgap, turning the defects into effective trapping centers that greatly increase the recombination probability of charge carriers. From Table 3, it is seen that the defect densities of D1 and D2, i.e. V_{Sb} and Se_i , are almost identical for both devices. However, the defect density of D3, i.e. Se_{Sb} of the 20 min-Sb₂Se₃ device is one order of magnitude larger than that of the 15min-Sb₂Se₃ device. We attribute the massive antisite defects to over extended annealing duration for the 20 min-Sb₂Se₃ devices. Based on DFT calculations, when subjected to high temperature, Se atoms are prone to substitute Sb atoms thermodynamically under Se rich

environment. Such a large amount of antisite defects with deep energy level will act as recombination centers and significantly affect photovoltaic performance of the device.

4. Conclusion

In summary, Sb_2Se_3 thin film solar cells were fabricated by an effective combination reaction of sputtered Sb metallic precursors. A champion device with a highly interesting PCE of 6.15 % that represents the highest efficiency of sputtered Sb_2Se_3 solar cells has been successfully obtained. Self-assembled growth of Sb_2Se_3 thin films consist of large grains with excellent continuity across the whole films was achieved via this combination reaction. Highly-crystallized Sb_2Se_3 with the desired [221] preferred orientation, stoichiometric composition as well as an optimized $\text{Sb}_2\text{Se}_3/\text{CdS}$ heterojunction were obtained under a proper selenization scenario. Moreover, by utilizing the Sb metallic precursors for post-selenization heat treatment, the thickness of the interfacial MoSe_2 layer between the Mo substrate and Sb_2Se_3 light absorber layer could be efficiently tailored. Our DFT simulation results further confirmed that Se vapor would be prone to react with the Sb lattice energetically, therefore an over-thick disadvantageous MoSe_2 layer that prevalently existed in Mo substrate coupled Sb_2Se_3 solar cells could be effectively prevented. As a result, the corresponding FF of our champion device has dramatically increased from a poor value of 47% (in our previous work) to 59.5 % (in this work). In addition, a systematic investigation of interfacial properties and defect properties demonstrated that a suitable annealing duration is really beneficial for reducing deep defect density within the device. Nevertheless, J_{SC} was found to be the major obstacle for our device when compared with those first-tier Sb_2Se_3 thin film solar cells where non-toxic or additional buffer layers were used. Comprehensive understanding of interface engineering would be urgently required to further improve the device efficiency in future work.

Acknowledgements

This work was supported by Key Project of Department of Education of Guangdong Province (No. 2018KZDXM059), Science and Technology plan project of Shenzhen (20190726221232961), National Natural Science Foundation of China (No. 61404086,

51802050, U1804160, 21603146), The Natural Science Foundation of Guizhou Province (Qian Ke He [2017]1064), The postgraduate innovation development fund project of Shenzhen University (PIDFP-ZR2019019), Shenzhen Key Lab Fund (ZDSYS 20170228105421966), Science and Technology plan project of Shenzhen (JCYJ20180305124340951). The authors wish to acknowledge the assistance on HAADF-STEM observation received from the Electron Microscope Center of the Shenzhen University.

References

- [1] Green, M. A. et al. Solar cell efficiency tables (version 51) Prog. Photovolt. Res. Appl. 26 (2018) 3–12.
- [2] Solar Frontier. Solar Frontier achieves world record thin-film solar cell efficiency of 22.9%. Solar. Frontier. http://www.solar-frontier.com/eng/news/2017/1220_press.html (2017) Accessed June 2018.
- [3] Yang W S, Noh J H, Jeon N J, et al. High-performance photovoltaic perovskite layers fabricated through intramolecular exchange. Science 348(6240) (2015) 1234-1237.
- [4] Chen, C. et al. Characterization of basic physical properties of Sb_2Se_3 and its relevance for photovoltaics. Front. Optoelectron. 10 (2017) 18-30.
- [5] Yuan, C, et al. Rapid thermal process to fabricate Sb_2Se_3 thin film for solar cell application. Sol. Energy 137 (2016) 256-260.
- [6] Shen, K. et al. Mechanisms and modification of nonlinear shunt leakage in Sb_2Se_3 thin film solar cells, Sol. Energy Mater. Sol. Cells 186 (2018) 58-65.
- [7] Zhou, Y. et al. Thin-film Sb_2Se_3 photovoltaics with oriented one-dimensional ribbons and benign grain boundaries. Nat. Photon. 9 (2015) 409-415.
- [8] Zhou, Y. et al. Solution-processed antimony selenide heterojunction solar cells. Adv. Energy Mater. 4 (2014) 1079-1083.
- [9] Guo H. F, et al. Significant increase in efficiency and limited toxicity of a solar cell based on Sb_2Se_3 with SnO_2 as a buffer layer. J. Mater. Chem. C 7(45) (2019) 14350-14356.
- [10] Wang, W. et al. Over 6% Certified $\text{Sb}_2(\text{S},\text{Se})_3$ solar cells fabricated via in situ hydrothermal growth and post-selenization, Adv. Electron Mater. 5 (2018) 1800683.
- [11] Cheng, J, et al. Air Stable Solar Cells with 0.7 V Open Circuit Voltage Using Selenized Antimony Sulfide Absorbers Prepared by Hydrazine Free Solution Method. Sol. RRL 3(5) (2019) 1800346.
- [12] Liu, X. et al. Thermal evaporation and characterization of Sb_2Se_3 thin film for substrate $\text{Sb}_2\text{Se}_3/\text{CdS}$ solar cells. ACS Appl. Mater. Interfaces 6 (2014) 10687–10695.

- [13] Leng, M. et al. Selenization of Sb_2Se_3 absorber layer: an efficient step to improve device performance of $\text{CdS}/\text{Sb}_2\text{Se}_3$ solar cells. *Appl. Phys. Lett.* 105 (2014) 083905.
- [14] Liu, X. et al. Improving the performance of Sb_2Se_3 thin film solar cells over 4% by controlled addition of oxygen during film deposition. *Prog. Photo. Res. Appl.* 23 (2015) 1828–1836.
- [15] Wang, L. et al. Stable 6%-efficient Sb_2Se_3 solar cells with a ZnO buffer layer. *Nat. Energy* 2 (2017) 17046.
- [16] Wen, X. et al. Vapor transport deposition of antimony selenide thin film solar cells with 7.6% efficiency. *Nat. Commun.* 9 (2018) 2179.
- [17] Hu, X. B. et al. Improving the efficiency of Sb_2Se_3 thin-film solar cells by post annealing treatment in vacuum condition. *Sol. Energy Mater. Sol. Cells* 187 (2018) 170-175.
- [18] Tao, J. et al. Solution-processed SnO_2 interfacial layer for highly efficient Sb_2Se_3 thin film solar cells. *Nano Energy* 60 (2019) 802-809.
- [19] Li, Z. Q. et al. 9.2%-efficient core-shell structured antimony selenide nanorod array solar cells. *Nat. Commun.* 10 (2019) 125.
- [20] Li, D. et al. Stable and efficient $\text{CdS}/\text{Sb}_2\text{Se}_3$ solar cells prepared by scalable close space sublimation. *Nano Energy* 49 (2018) 346-353.
- [21] Liang, G. X. et al. Facile preparation and enhanced photoelectrical performance of Sb_2Se_3 nano-rods by magnetron sputtering deposition. *Sol. Energy Mater. Sol. Cells* 160 (2017) 257-262.
- [22] Liang, G. X. et al. Thermally induced structural evolution and performance of Sb_2Se_3 films and nanorods prepared by an easy sputtering method. *Sol. Energy Mater. Sol. Cells* 174 (2018) 263–270.
- [23] Li, G et al. Improvement in Sb_2Se_3 Solar Cell Efficiency through Band Alignment Engineering at the Buffer/Absorber Interface. *Appl. Mater. Interfaces* 11 (2019) 828–834.
- [24] Shi, J. H. et al. Fabrication of $\text{Cu}(\text{In,Ga})\text{Se}_2$ thin films by sputtering from a single quaternary chalcogenide target. *Prog. Photovolt. Res. Appl.* 19(2) (2011) 160-164.
- [25] Yan, C. et al. $\text{Cu}_2\text{ZnSnS}_4$ solar cells with over 10% power conversion efficiency enabled by heterojunction heat treatment. *Nat Energy* 3(9) (2018) 764.
- [26] Chawla et al. Effect of composition on high efficiency CZTSSe devices fabricated using co-sputtering of compound targets. In 2012 38th IEEE Photovoltaic Specialists Conference (2012) 002990-002992. IEEE.
- [27] Tang, R, et al. Highly efficient and stable planar heterojunction solar cell based on sputtered and post-selenized Sb_2Se_3 thin film. *Nano Energy* 64 (2019) 103929.

- [28] Ganchev, M, et al. Preparation of Cu(In,Ga)Se₂ layers by selenization of electrodeposited Cu–In–Ga precursors. *Thin Solid Films* 511 (2006) 325-327.
- [29] Yao, L, et al. CZTSe solar cells prepared by electrodeposition of Cu/Sn/Zn stack layer followed by selenization at low Se pressure. *Nanoscale Res Lett.* 9(1) (2014) 678.
- [30] Salomé, P. M. P., et al. Growth and characterization of Cu₂ZnSn(S, Se)₄ thin films for solar cells. *Sol. Energy Mater. Sol. Cells* 101 (2012) 147-153.
- [31] Kresse, G. Furthmüller, J., Efficient Iterative Schemes for Ab Initio Total-Energy Calculations Using a Plane-Wave Basis Set. *Phys. Rev. B* 54 (1996) 11169–11186.
- [32] Kresse, G. Furthmüller, J., Efficiency of Ab-Initio Total Energy Calculations for Metals and Semiconductors Using a Plane-Wave Basis Set. *Comp. Mater. Sci.* 6 (1996) 15–50.
- [33] Blöchl, P. E., Projector Augmented-Wave Method. *Phys. Rev. B* 50 (1994) 17953–17979.
- [34] Kresse, G. Joubert, D., From Ultrasoft Pseudopotentials to the Projector Augmented-Wave Method. *Phys. Rev. B* 59 (1999) 1758–1775.
- [35] Perdew, J. P. Burke, K. Ernzerhof, M., Generalized Gradient Approximation Made Simple. *Phys. Rev. Lett.* 77 (1996) 3865-3868.
- [36] Monkhorst, H. J. Pack, J. D., Special Points for Brillouin-Zone Integrations. *Phys. Rev. B* 13 (1976) 5188-5192.
- [37] Ross, R. G. Hume-Rothery, W, High Temperature X-Ray Metallography: I. A New Debye-Scherrer Camera for Use at Very High Temperatures Ii. A New Parafocusing Camera Iii. Applications to the Study of Chromium, Hafnium, Molybdenum, Rhodium, Ruthenium and Tungsten. *J. Less Common Metals*, 5 (1963) 258-270.
- [38] Schiferl, D., 50-Kilobar Gasketed Diamond Anvil Cell for Single-Crystal X-Ray Diffractometer Use with the Crystal Structure of Sb up to 26 Kilobars as a Test Problem. *Rev. Sci. Instrum.* 48 (1977) 24-30.
- [39] Su, Z.H, et al. Fabrication of Cu₂ZnSnS₄ solar cells with 5.1% efficiency via thermal decomposition and reaction using a non-toxic sol–gel route. *J. Mater. Chem. A* 2(2) (2014) 500-509.
- [40] Li, J. J, et al. A temporary barrier effect of the alloy layer during selenization: tailoring the thickness of MoSe₂ for efficient Cu₂ZnSnSe₄ solar cells. *Adv. Energy Mater.* 5(9) (2015) 1402178.
- [41] Sites JR, et al. Diode quality factor determination for thin-film solar cells. *Sol. Cells* 27 (1989) 411–417.
- [42] Ishaq, M., et al. Efficient Double Buffer Layer Sb₂(Se_xS_{1-x})₃ Thin Film Solar Cell Via Single Source Evaporation. *Sol. RRL*, 2(10) (2018) 1800144.

- [43] Chirila, A. et al. Highly efficient Cu(In,Ga)Se₂ solar cells grown on flexible polymer films. Nat. mater. 10 (2011) 857-861.
- [44] Li, J. J, et al. 10% Efficiency Cu₂ZnSn(S,Se)₄ thin film solar cells fabricated by magnetron sputtering with enlarged depletion region width. Sol. Energy Mater. Sol. Cells 149 (2016) 242-249.
- [45] Li, Z. Q, et al. Sb₂Se₃ thin film solar cells in substrate configuration and the back contact selenization. Sol. Energy Mater. Sol. Cells 161 (2017) 190-196.
- [46] Liu, S. C, et al. GeSe thin-film solar cells. Mater. Chem. Front. (2020) <https://doi.org/10.1039/c9qm00727j>
- [47] Hu, X. B, et al. Investigation of electrically-active defects in Sb₂Se₃ thin-film solar cells with up to 5.91% efficiency via admittance spectroscopy. Sol. Energy Mater. Sol. Cells. 186 (2018) 324-329.
- [48] Li, J. J, et al. Tailoring the defects and carrier density for beyond 10% efficient CZTSe thin film solar cells. Sol. Energy Mater. Sol. Cells. 159 (2017) 447-455.
- [49] Liu, X. S. et al. Enhanced Sb₂Se₃ solar cell performance through theory-guided defect control. Prog. Photovolt. Res. Appl. 25 (10) (2017) 861-870.
- [50] Guo, H. F. et al. Enhancement in the Efficiency of Sb₂Se₃ Thin Film Solar Cells by Increasing Carrier Concentration and Inducing Columnar Growth of the Grains. Sol. RRL 3 (3) (2019): 1800224.

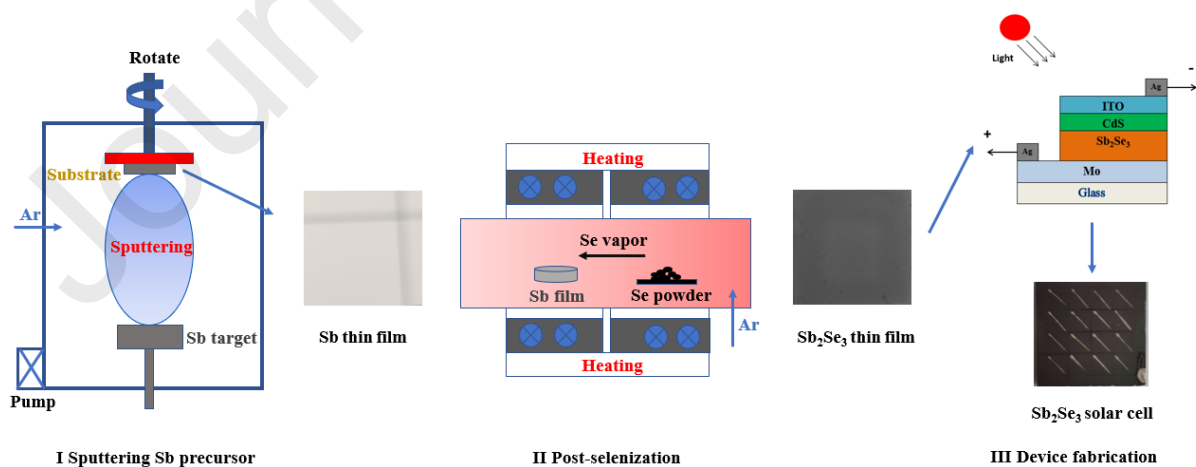


Figure 1. Schematic diagram of the Sb₂Se₃ device fabrication.

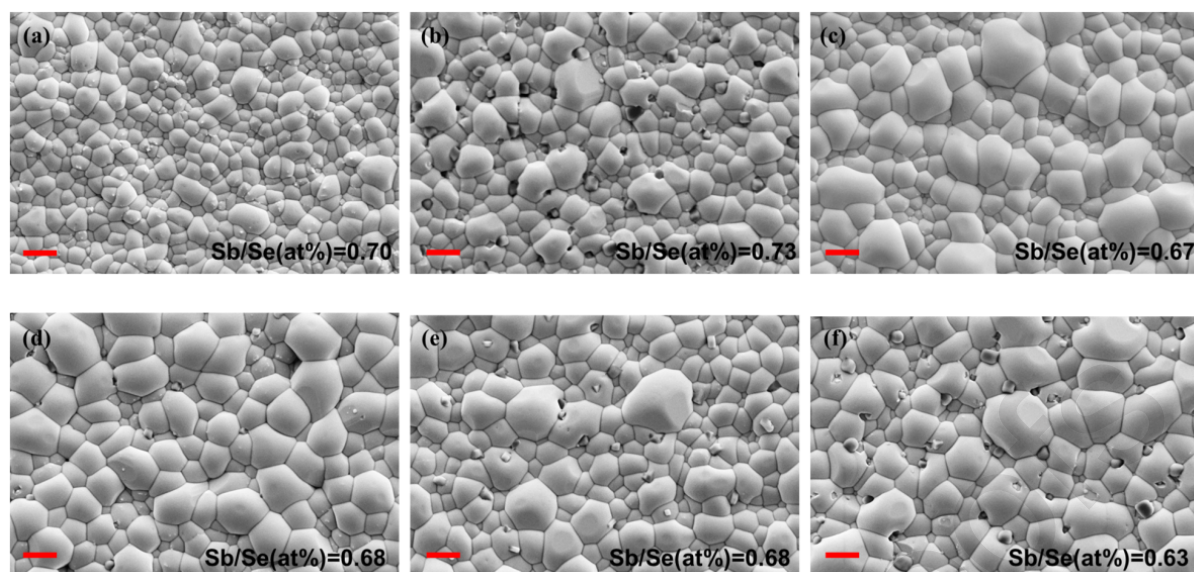


Figure 2. Surface morphologies of the Sb_2Se_3 thin films with different selenization durations. SEM top-view images of Sb metallic precursor selenized at 400 °C for 5 min (a), 10 min (b), 15 min (c), 20 min (d), 25 min (e) and 30 min (f). The red scale bar at the left bottom corner of each figure reads 1 μm .

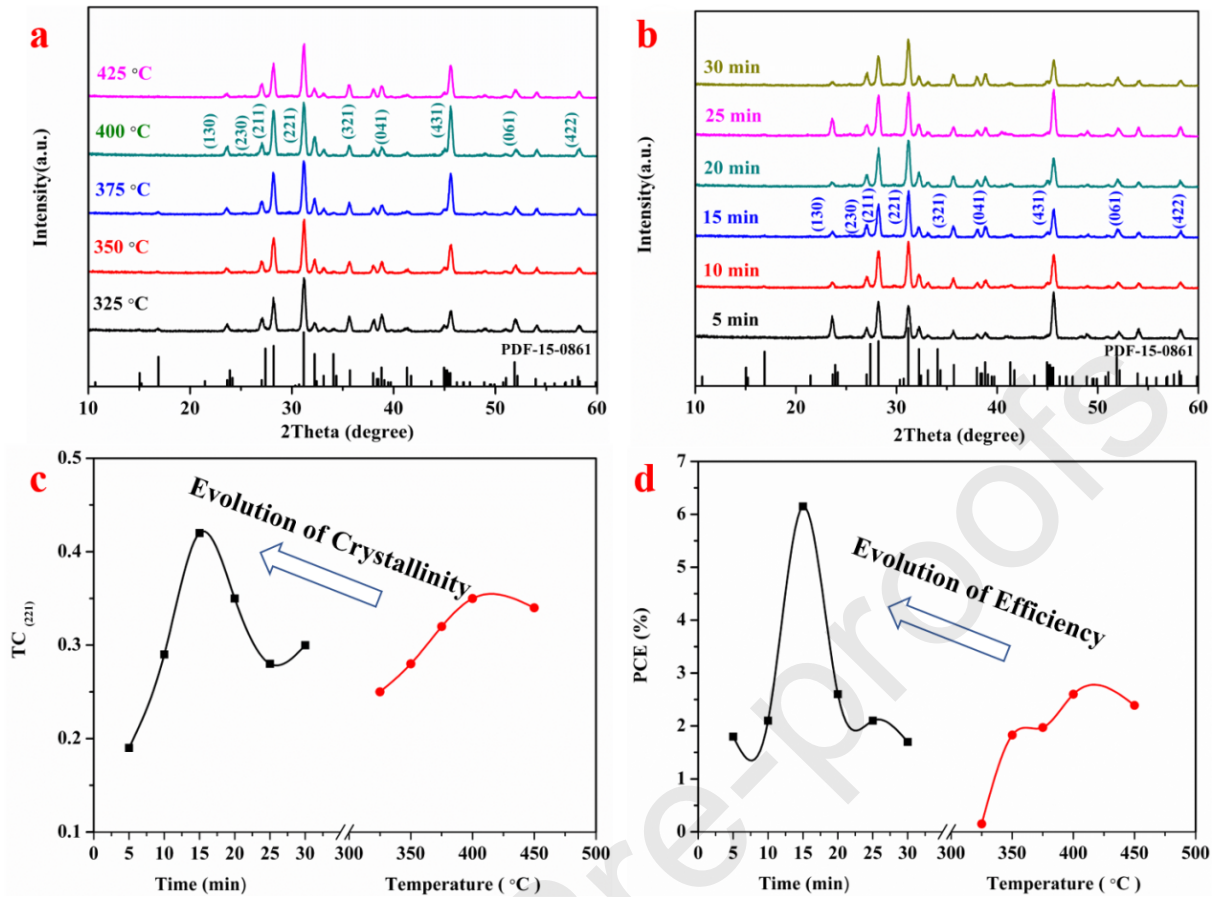


Figure 3. Morphology evolutions of the Sb_2Se_3 thin films. XRD data of Sb_2Se_3 thin films annealed by using different selenization temperatures (a) and durations (b). Texture coefficients (TC) of (221) diffraction peaks (c) and PCE (d) of the Sb_2Se_3 thin film devices fabricated via various selenization scenarios.

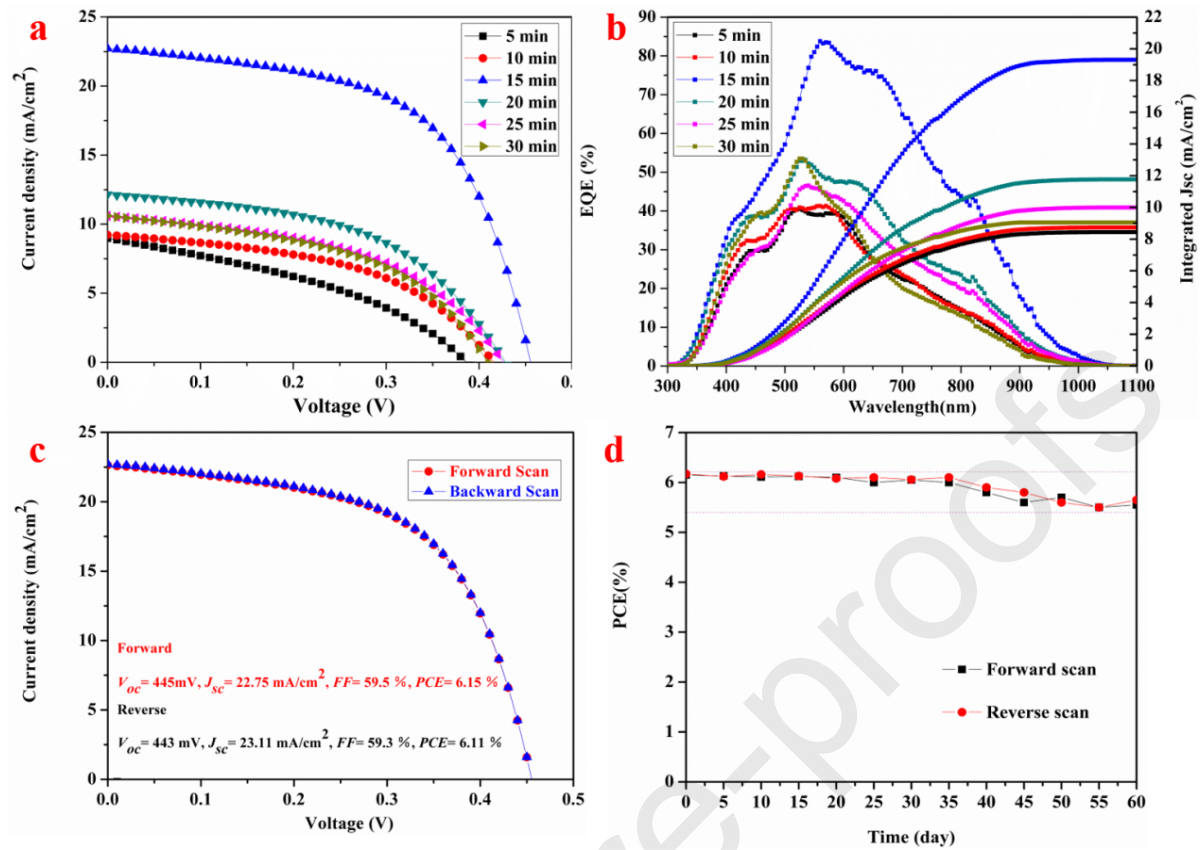


Figure 4. Device performance. Current density-voltage (J - V) curves (a), external quantum efficiency (EQE) and integrated J_{SC} (b) of Sb_2Se_3 devices fabricated by using different selenization durations. Current density-voltage (J - V) curves from different scanning directions of the champion device (c). Device stability of the 15min- Sb_2Se_3 device after 1000 h storage in air ambient without special treatment/encapsulation (d).

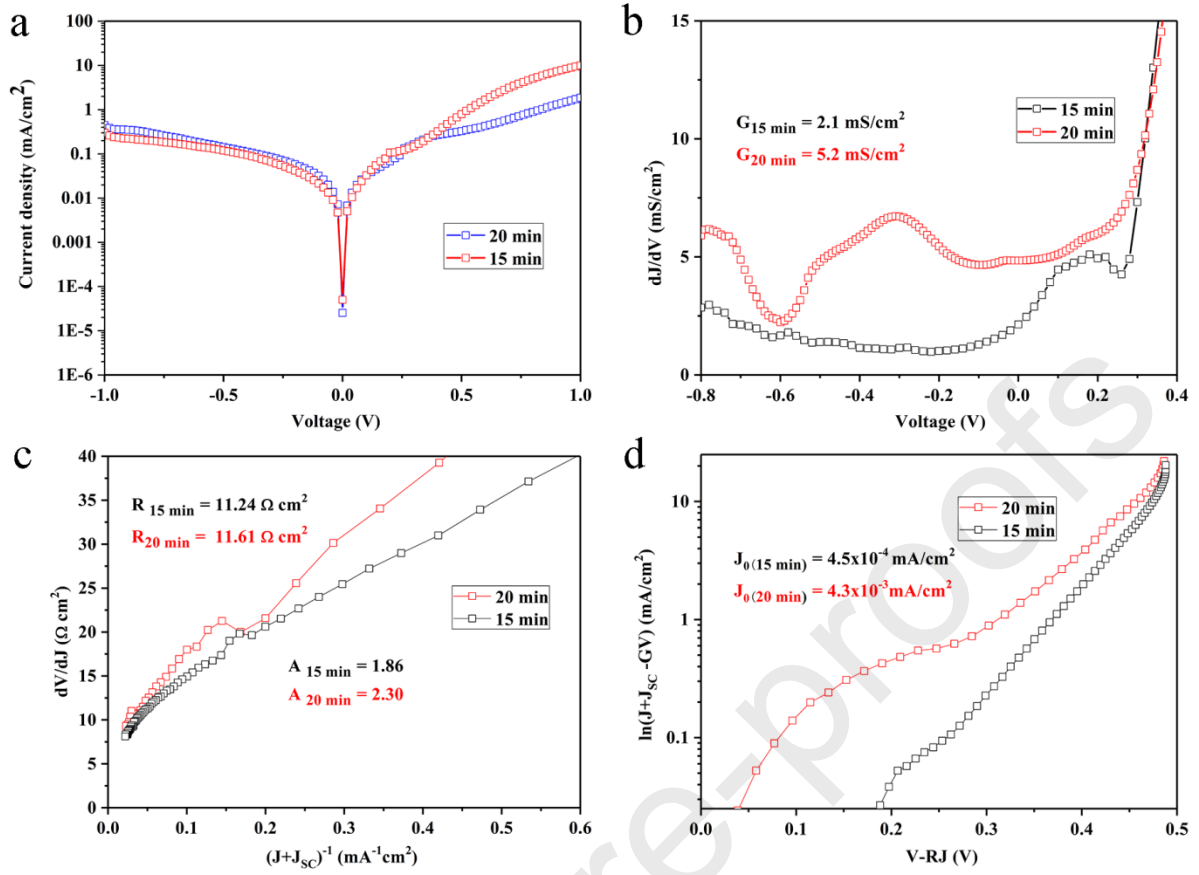


Figure 5. Dark J - V characteristics for the 15min-Sb₂Se₃ and 20min-Sb₂Se₃ devices. Dark J - V curves (a), shunt conductance G characterizations (b), series resistance R and ideality factor A characterizations (c) and reverse saturation current density J_0 characterizations (d) of the two devices.

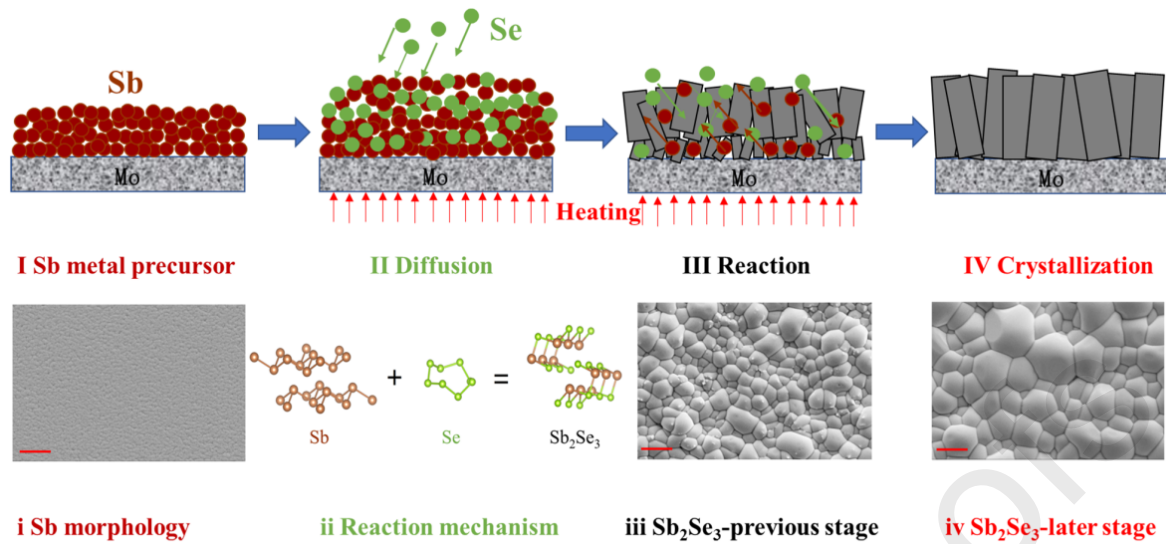


Figure 6. Crystallization procedures of Sb₂Se₃ thin films prepared via Sb metallic precursor selenization. The red scale bar at the left bottom corner of each SEM image reads 1 μm .

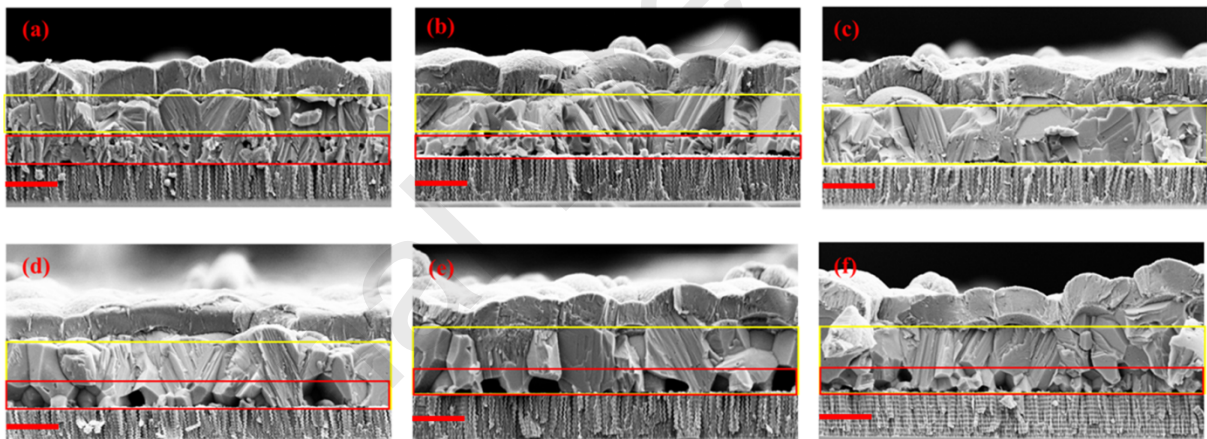


Figure 7. Cross-sectional microstructures of Sb₂Se₃ thin films with different selenization durations. SEM cross-sectional images of Sb metallic precursor selenized at 400 $^{\circ}\text{C}$ for 5 min (a), 10 min (b), 15 min (c), 20 min (d), 25 min (e) and 30 min (f). The red scale bar at the left bottom corner of each figure reads 1 μm .

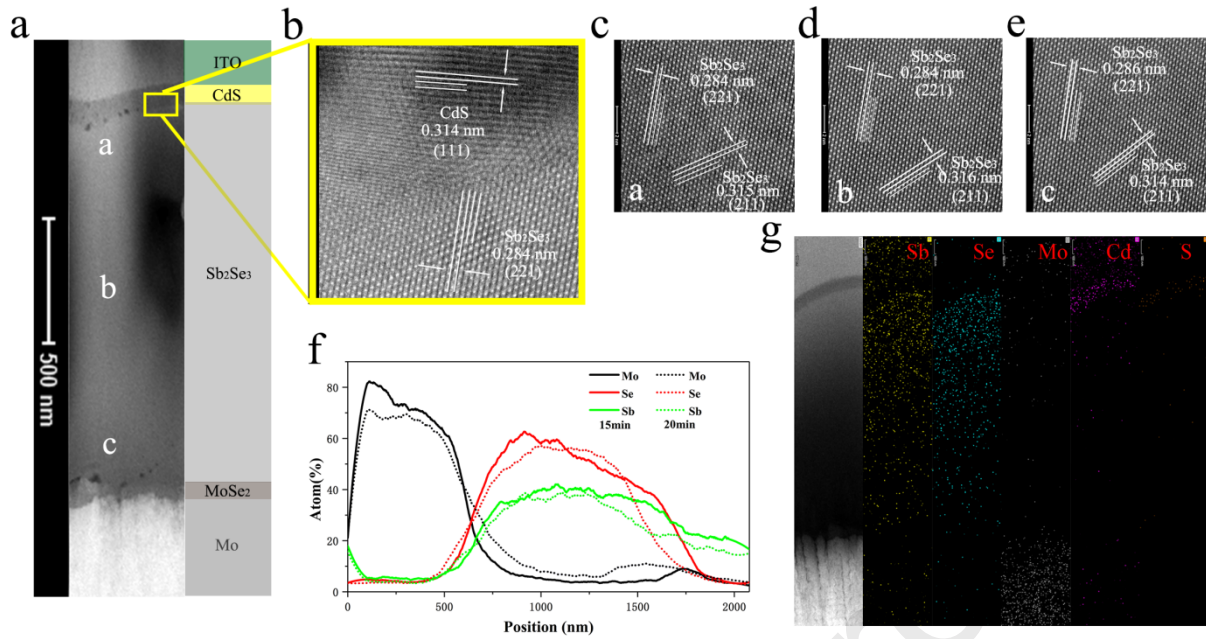


Figure 8. TEM characterization of the Sb_2Se_3 champion device. Cross-sectional TEM image of the Sb_2Se_3 champion device (a). HRTEM image of the $\text{Sb}_2\text{Se}_3/\text{CdS}$ interface (b). Lattice fringes of three arbitrary spots a, b and c across the Sb_2Se_3 thin film in (a) performed by HRTEM are shown in (c), (d) and (e), correspondingly. EDS elemental profiles across the device (f), HAADF-STEM image and EDS elemental mapping (g) of the device.

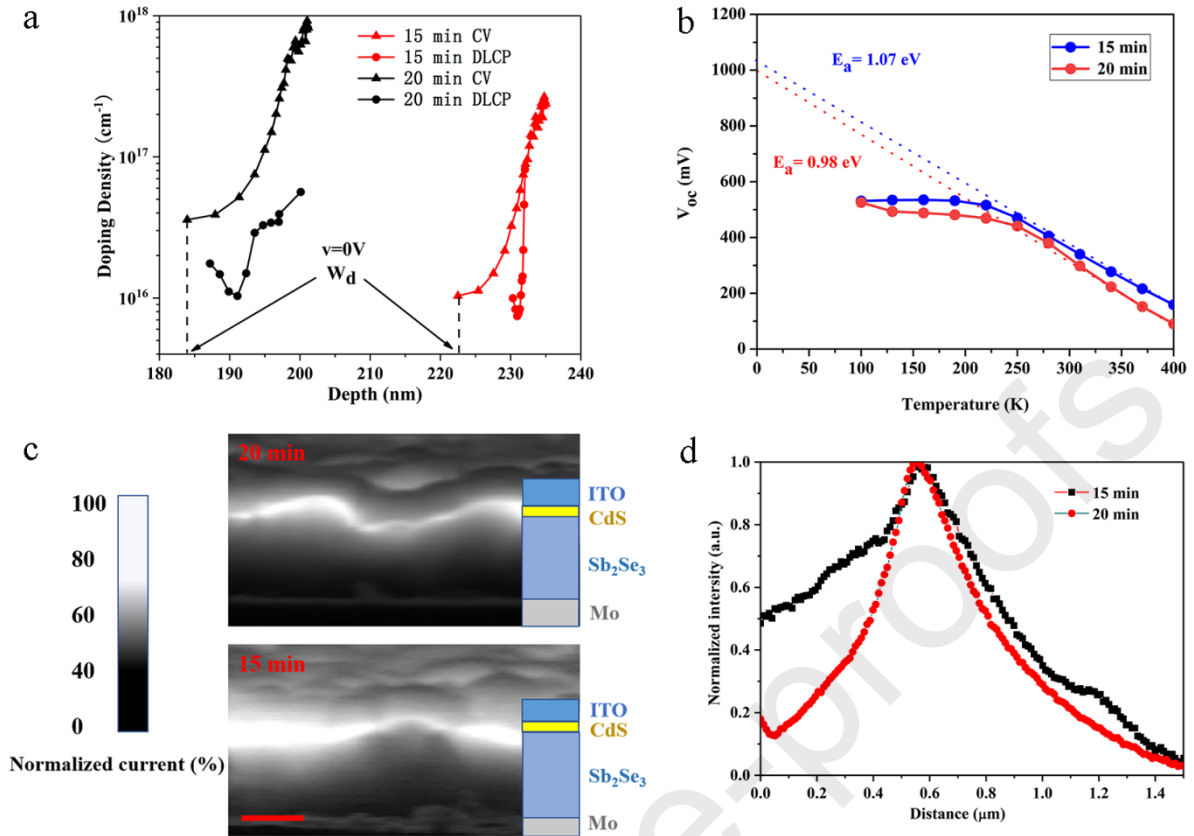


Figure 9. $\text{Sb}_2\text{Se}_3/\text{CdS}$ interfacial defect characterizations and EBIC analyses of devices. *CV* and *DLCP* profiling (a), temperature-dependent open circuit voltage measurements (b), EBIC images (c) and the EBIC signal intensity profiling (d) of the 15min- Sb_2Se_3 and 20min- Sb_2Se_3 devices. The red scale bar at the left bottom corner of Figure 9(c) reads 1 μm .

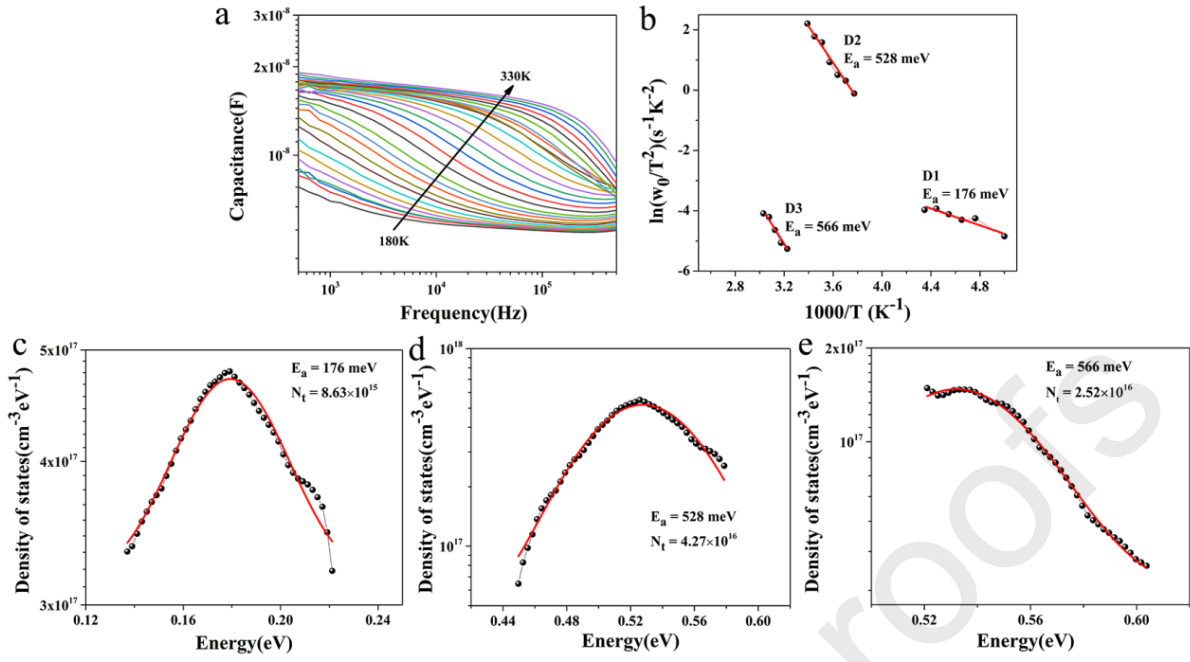


Figure 10. Temperature-dependent admittance analyses of the champion device. Capacitance-frequency-temperature (C - f - T) spectra (a) and defect activation energies (b) of the 15min-Sb₂Se₃ device. Defect distributions of D1 (c), D2 (d) and D3 (e) of the 15min-Sb₂Se₃ device derived from the admittance spectra.

Table 1. Device performance parameters of the Sb_2Se_3 device with different selenization time

Samples	V_{oc} (mV)	J_{sc} (mA/cm ²)	FF (%)	E_{ff} (%)
5 min	390	9.00	37.0	1.32
10 min	420	9.23	48.0	1.84
15 min	455	22.75	59.5	6.15
20 min	430	12.16	49.8	2.60
25 min	430	10.6	47.5	2.16
30 min	410	10.6	47.8	2.07

Table 2. Summary of planar heterojunction Sb_2Se_3 solar cell with substrate configuration publications by different fabrication methods

Method	Device configuration	Eff (%)	V_{oc} (mV)	J_{ac} (mA/cm ²)	FF (%)	Ref.
Co-eva ^{a)}	Mo/ Sb_2Se_3 /CdS/ZnO/AZO/Ag	4.25	427	17.11	58.15	Mai [45]
CSS ^{b)}	Mo/ Sb_2Se_3 /Cd _x Zn _{1-x} S/ZnO/AZO	6.71	403	25.69	64.78	Mai [23]
Sput ^{c)}	Mo/ Sb_2Se_3 /CdS/ZnO/AZO/Ag	3.35	437	15.93	48	Liang [21]
Sput-Se ^{d)}	Mo/ Sb_2Se_3 /CdS/ITO/Ag	6.06	494	25.91	47.7	Liang [27]
Sput-Sb-Se (RTP) ^{e)}	Mo/ Sb_2Se_3 /CdS/ZnO/AZO/Al	3.47	414	16.0	52	Zhu [5]
Sput-Sb-Se (NTP) ^{f)}	Mo/ Sb_2Se_3 /CdS/ITO/Ag	6.15	455	22.75	59.5	This work

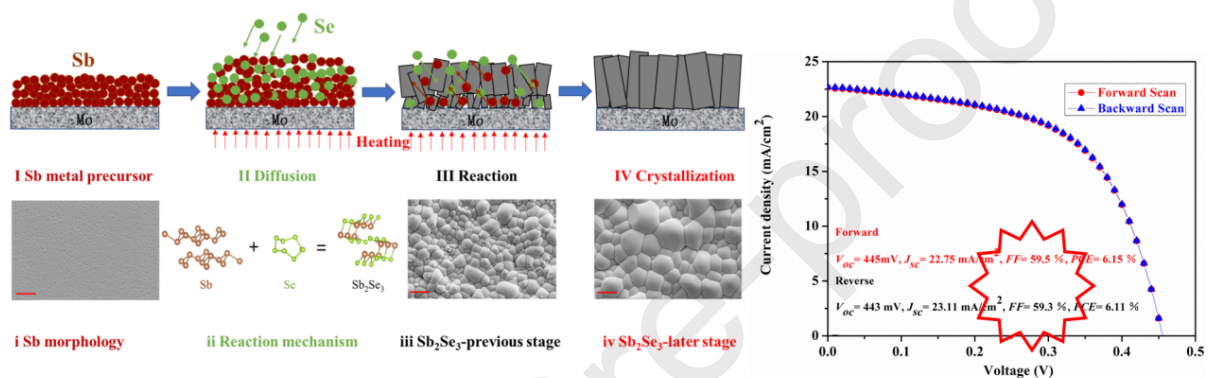
^{a)} Co-evaporation. ^{b)} Closed space sublimation. ^{c)} Sputtering Sb_2Se_3 . ^{d)} Sputtering Sb_2Se_3 and post-selenization. ^{e)} Sputtering Sb and post-selenization with Rapid Thermal Process. ^{f)} Sputtering Sb and post-selenization with Normal Thermal Process.

Table 3. Defect parameters of the 15 min- Sb_2Se_3 and 20 min- Sb_2Se_3 devices characterized by admittance spectroscopy

	D1		D2		D3	
	E_a (meV)	N_t (cm ⁻³)	E_a (meV)	N_t (cm ⁻³)	E_a (meV)	N_t (cm ⁻³)
15 min- Sb_2Se_3	176	8.6×10^{15}	528	4.3×10^{16}	566	2.5×10^{16}
20 min- Sb_2Se_3	181	1.1×10^{16}	496	3.6×10^{16}	593	2.3×10^{17}

Table of contents: An effective combination reaction involved with sputtered and selenized Sb precursor was used for preparing Sb_2Se_3 thin film solar cells. Self-assembled growth of Sb_2Se_3 with large crystal grains, benign orientation, stoichiometric composition and high-quality heterojunction interface. A champion device with PCE of 6.15 % is comparable to the state-of-the-art devices and represents the highest efficiency of sputtered Sb_2Se_3 solar cells.

ToC figure



An effective combination reaction of sputtered and selenized Sb with high FF Sb_2Se_3 solar cells

Supporting Information

An effective combination reaction involved with sputtered and selenized Sb precursors for efficient Sb_2Se_3 thin film solar cells

Yan-Di Luo^{1#}, Rong Tang^{1#}, Shuo Chen^{1#}, Ju-Guang Hu¹, Yi-Ke Liu², Ying-Fen Li², Xin-Sheng Liu³, Zhuang-Hao Zheng¹, Zheng-Hua Su¹, Xiu-Fang Ma¹, Ping Fan¹, Xiang-Hua Zhang⁴, Hong-Li Ma⁴, Zhi-Gang Chen⁵, Guang-Xing Liang^{1*}

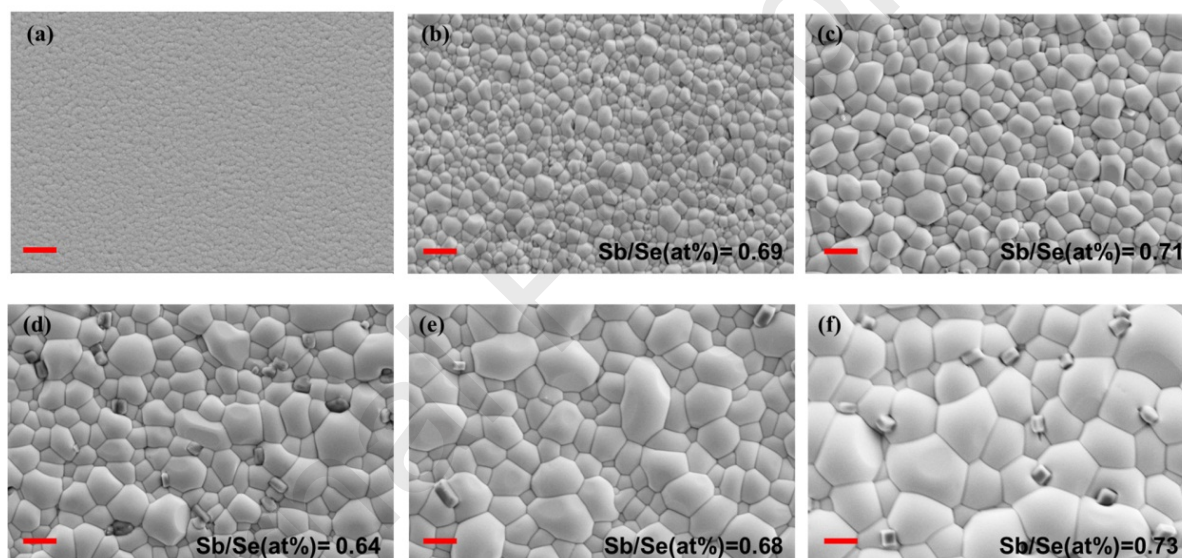


Figure S1. Surface morphologies of the Sb_2Se_3 thin films with different selenization temperatures. SEM top-view images of Sb metallic precursor (a), and selenized at 325 °C (b), 350 °C (c), 375 °C (d), 400 °C (e) and 425 °C (f). The red scale bar at the left bottom corner of each figure reads 1 μm .

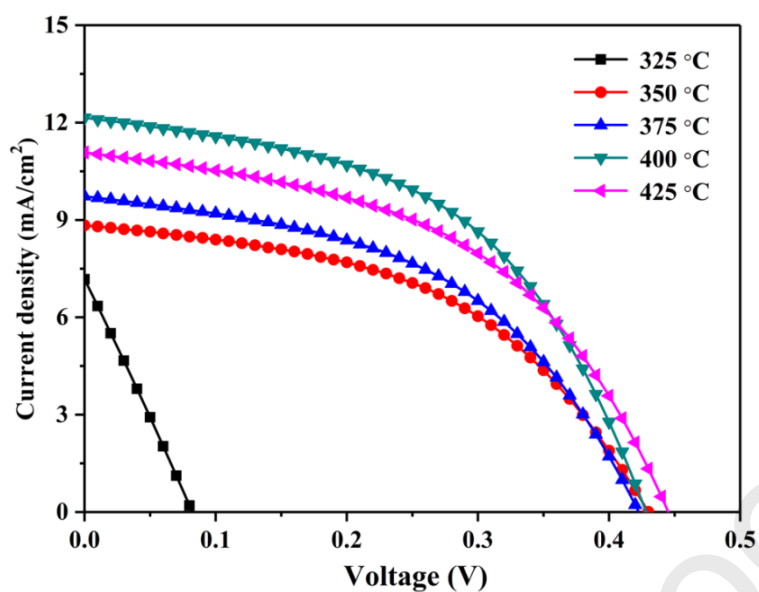


Figure S2. Current density-voltage (J - V) curves of Sb_2Se_3 devices fabricated at different selenization temperatures.

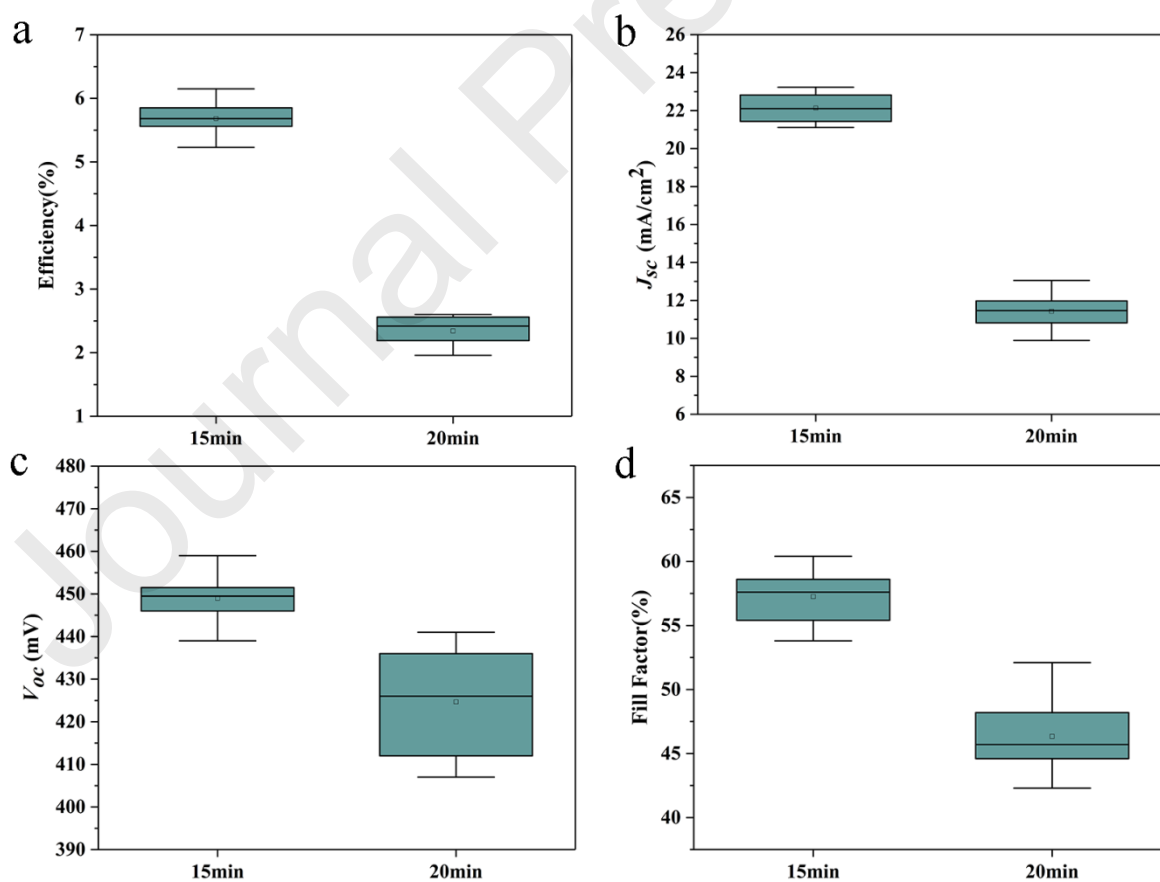


Figure S3. Main parameters of the 15- Sb_2Se_3 and 20- Sb_2Se_3 devices

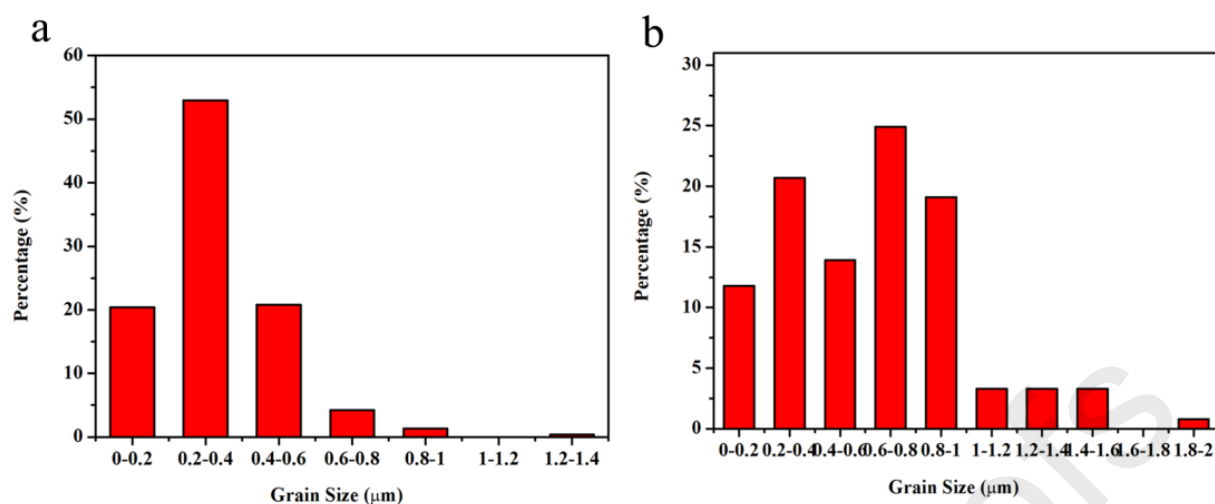


Figure S4. Grain size distributions of Sb_2Se_3 thin films at the early stage (a) and later stage (b) of selenization.

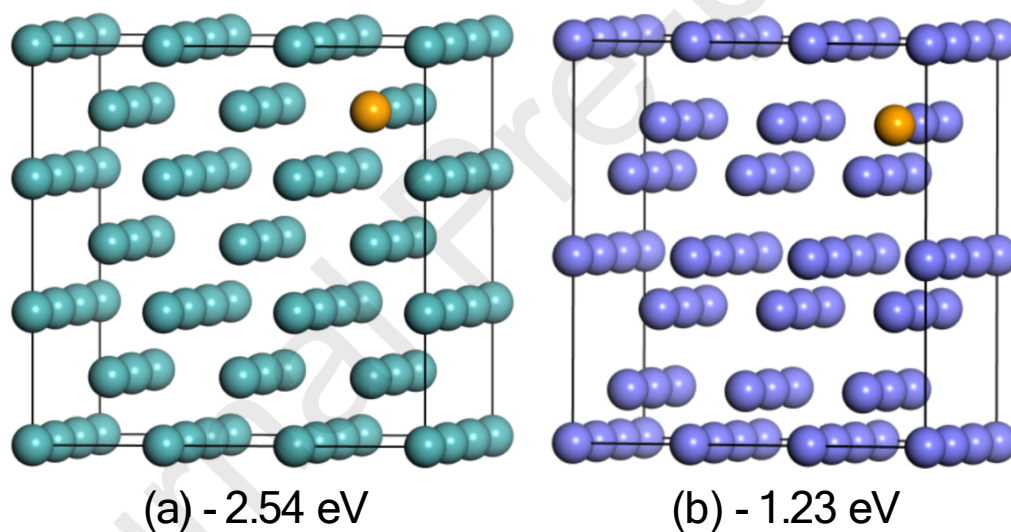


Figure S5. The schematic structures of bulk Mo (a) and Sb (b) system, in which 1/54 bulk atoms were substituted by Se atoms. The black line denotes the periodic supercell used in DFT calculations, and the corresponding energy change due to the substitution by Se was listed below. The green, orange and purple balls represent Mo, Se and Sb atoms, respectively.

Table S1. Device performance parameters of the Sb_2Se_3 devices with different selenization temperatures

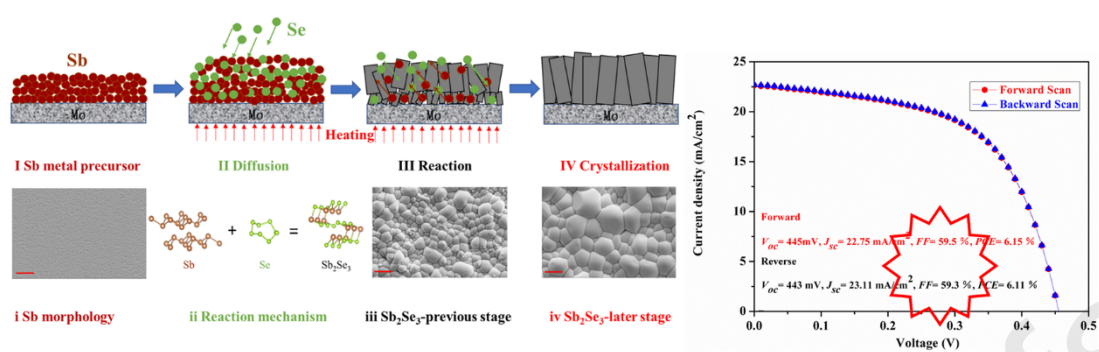
Samples	V_{oc} (mV)	J_{sc} (mA/cm ²)	FF (%)	E_{ff} (%)
325°C	80	7.18	27.0	0.15
350 °C	430	8.84	48.0	1.83
375 °C	420	9.74	48.2	1.97
400 °C	430	12.16	49.8	2.60
425 °C	450	11.08	48.0	2.39

Declaration of interests

The authors declare that they have no known competing financial interests or personal relationships that could have appeared to influence the work reported in this paper.

The authors declare the following financial interests/personal relationships which may be considered as potential competing interests:

- ✧ **An effective combination reaction of Sb metallic precursors for efficient Sb_2Se_3 solar cell**
- ✧ **Self-assembled growth of stoichiometric Sb_2Se_3 thin film with desired orientation**
- ✧ **An over-thick MoSe_2 interfacial layer could be effectively suppressed**
- ✧ **The highest PCE of 6.15 % in sputtered Sb_2Se_3 thin film solar cell with excellent stability**



An effective combination reaction of sputtered and selenized Sb with high FF Sb₂Se₃ solar cells